Top Catal (2017) 60:503–512
DOI 10.1007/s11244-016-0708-6

ORIGINAL PAPER

Comparative Analysis of Cobalt Oxide Nanoisland Stability and Edge Structures on Three Related Noble Metal Surfaces: Au(111), Pt(111) and Ag(111)

Jakob Fester[1] · Michal Bajdich[2] · Alex S. Walton[1,3] · Z. Sun[1] · Philipp N. Plessow[2] · Aleksandra Vojvodic[2] · Jeppe V. Lauritsen[1]

Published online: 12 September 2016

Abstract Metal oxide nanostructures and thin films grown on metallic substrates have attracted strong attention as model catalysts and as interesting inverse catalyst systems in their own right. In this study, we investigate the role of metal support in the growth and stabilization of cobalt oxide nanostructures on the three related (111) surfaces of Au, Pt and Ag, as investigated by means of high-resolution scanning tunneling microscopy and DFT calculations. All three substrates promote the growth of crystalline CoO_x ($x = 1-2$) islands under oxidative conditions, but we find several noteworthy differences in the occurrence and stabilization of four distinct cobalt oxide island phases: Co–O bilayers, O–Co–O trilayers, Co–O–Co–O double bilayers and O–Co–O–Co–O multilayers. Using atom-resolved images combined with analysis of defect lines in bilayer islands on Au and Pt, we furthermore unambiguously determine the edge structure. Interestingly, the island shape and abundances of edge types in bilayers change radically from mixed Co/O edge terminations on Au(111) to a predominance of Co terminated edges (~91 %) on Pt(111) which is especially interesting since the Co metal edges are expected to host the most active sites for water dissociation.

Keywords Scanning tunneling microscopy Density functional theory Cobalt oxides Pt(111) Au(111) Ag(111) Inverse oxide/metal catalyst · Water dissociation

1 Introduction

Among a variety of applications, cobalt oxides have recently attracted considerable attention due to their potential use as earth-abundant heterogeneous catalysts for, especially, low temperature CO oxidation [1, 2] and the oxygen evolution reaction—one of the half reactions in electrochemical water splitting ($2H_2O \rightarrow O_2 + 4H^+ + 4e^-$) [3–5], in both cases replacing expensive noble metals such as Pt and Ir. The fundamental working principles of cobalt oxide catalysts are different from their noble metal counterparts and not fully understood. However, it is known that the catalytic activity has a high dependency on the detailed oxide nanostructure, as encountered in numerous studies [6]. Defects, crystal facets as well as other nanoscale properties (particle edges etc.,) play a crucial role in the catalytic behavior, and the optimization often relies on the distribution and abundance of the active sites as exemplified in the case of fabrication of nanorods exposing the (110) planes of spinel Co_3O_4 with outstanding CO oxidation properties [1], as well as exfoliation of a bulk oxyhydroxide into freestanding β-CoOOH nanosheets catalyzing the OER reaction with activities competitive with the best known IrO_2 catalyst [4]. Furthermore, synergistic effects with Au [7, 8] and promotion by addition of other transition metals (Ni, Fe, Mn) [4, 9, 10] for

Electronic supplementary material The online version of this article (doi:10.1007/s11244-016-0708-6) contains supplementary material, which is available to authorized users.

✉ Jeppe V. Lauritsen
jvang@inano.au.dk

[1] Interdisciplinary Nanoscience Center (iNANO), Aarhus University, 8000 Aarhus C, Denmark

[2] SUNCAT Center for Interface Science and Catalysis, SLAC National Accelerator Laboratory, 2575 Sand Hill Road, Menlo Park, CA 94025, USA

[3] School of Chemistry, University of Manchester, Manchester M13 9PL, UK

the OER reaction, as well as synergistic effects with Pt in CO oxidation [11, 12], has been shown to increase the activity.

Preparation of cobalt oxides under vacuum conditions enables atomic-scale investigations and detailed characterization using a variety of surface science techniques, and the structural evolution and oxidation of cobalt oxide thin films has been studied on several single metal substrates, including Ir(100) [13, 14], Pd(100) [15], Pt(111) [16] and Au(111) [17–19]. Such systems have previously been used to study catalytic processes, e.g. CO activation on Co_3O_4 thin films [20]. Furthermore, metal oxides grown on noble metal substrates are interesting systems in their own right [21, 22], exemplified by the unraveling of interface confined ferrous centers for catalytic oxidation in FeO islands supported on Pt(111) [23], and demonstration of high reactivity for the water gas shift (WGS) reaction taking place at the metal-oxide interface in the CeO_x and TiO_x on Au(111) system [24].

Here, we compare the growth of cobalt oxide nanoislands on three different (111) surfaces of the noble metals Au, Pt and Ag to study the impact of the substrate on the cobalt oxide island morphology, as assessed by atom-resolved STM and compared to DFT stability calculations. We study the island formation in two oxygen pressure regimes (1×10^{-6} mbar O_2 and $>1 \times 10^{-5}$ mbar O_2 respectively) and find several interesting modifications in island shapes and stabilities originating from the choice of substrate. Furthermore, to reveal the edge structure and assign edge types in STM images of Co–O bilayers, we take advantage of a recent analysis performed on the similar FeO/Pt system [25, 26], building on observations of defect lines in the basal plane oxygen lattice.

2 Methods

2.1 Experimental Methods

The scanning tunneling microscopy (STM) studies were performed in UHV chambers with a base pressure below 1×10^{-10} mbar and using an Aarhus STM capable of atomic resolution imaging on a routine basis [27]. All the STM images were acquired at room temperature (300 K). Polished single crystals of Au, Pt and Ag cut in the (111) termination were cleaned by repeated sputtering (1.5 kV Ar^+) and annealing cycles. Cleanliness was assessed using both atom-resolved STM and laboratory X-ray photoelectron spectroscopy (XPS) (Phiobos 100 and XR50 source from SPECS Gmbh).

Synthesis of cobalt oxides was carried out by reactive deposition of submonolayer amounts of Co metal onto the sample (heated to 380 K) in an oxygen atmosphere of 1×10^{-6} mbar O_2 using an e-beam evaporator (Oxford Applied Research, model EGCO4) and a deposition rate of $\sim$0.04ML/min. The cobalt coverage was in general 30–50 % of a monolayer (ML) with 1ML defined as the number of Au(111) surface atoms. The samples were post annealed 10 min at 523 K in 1×10^{-6} mbar O_2 (low oxygen pressure synthesis) or using a moveable doser tube brought into 1 mm distance from the sample yielding a local pressure in excess of 1×10^{-5} mbar O_2 (high oxygen pressure synthesis).

2.2 Computational Details

The energetics of the infinite Co-oxide layers supported on precious metals was obtained from density functional theory (DFT) calculations using the VASP code [28–30]. The adopted settings were nearly identical to our previous works [18, 31], where the PBE [32] functional together with the Hubbard-U method [33] ($U_{eff} = 1$ eV for Co atoms), standard energy cutoff of 500 eV and approximately constant k-point mesh of $9 \times 9 \times 9$ points per $p(1 \times 1 \times 1)$ cell were used in all calculations. Within this method, the obtained lattice constants for bulk CoO, Pt, Au, Ag were a = 4.249, 3.968, 4.157, 4.147 Å respectively.

The $p(2 \times 2)$ metal-oxide overlayers were placed in a commensurate fashion on $p(2 \times 2)$ 3-layer fcc-metal (111) slabs in the fcc stacking for bilayes and on-top stacking for trilayers. Because the measured lattice spacings in STM for bilayers are in fact larger than for the substrate, an expansion of a supported oxide film can result in a reduction of its rumpling and in turn impact the oxide|metal interface characteristics [34]. The structures were therefore recalculated at 10 % enlarged in-plane lattices, showing the same trends as for the original lattices (see Supplementary Fig. S1; Table S1). The metal-oxide and 1 layer of fcc-metal were allowed to relax with the maximum force threshold of 0.02 eV/Å, while at least 16 Å of vacuum was used to separate the layers together with dipole corrections to remove any periodic interactions. The calculated lowest magnetic structure for bilayers was the well-known row-wise Antiferromagnetic (AFM) structure [35] while trilayers preferred Ferromagnetic (FM)-ordering.

The surface energies of the supported Co-oxide films were calculated relative to DFT energy of the most stable oxide, bulk CoO, using a procedure developed by Reuter and Scheffler [36] as $\gamma(1 \times 1) = \left(E^{\mathrm{DFT}}_{\mathrm{CoO}_x+\mathrm{sup\,port}} - E^{\mathrm{DFT}}_{\mathrm{sup\,port}} - N_{\mathrm{CoO}} E^{\mathrm{DFT}}_{\mathrm{CoO}} - N_{\mathrm{O}} \mu_{\mathrm{O}}(T,p)\right)/N_A$, where E^{DFT} are the calculated total energies of supported oxide and support only and the N_{CoO}, N_O and refer to number of CoO and excess O units in the simulation cell normalized by number of units N_A per surface area. The chemical potential of oxygen gas $\mu_O(T, p)$ is conventionally referenced to $\mu_O(T = 0\ \mathrm{K}, p = 1\ \mathrm{Atm.}) = \frac{1}{2} E^{DFT}_{O_2}$. The oxygen reference

is obtained from the experimental enthalpy of water as $\frac{1}{2}E_{O_2}^{DFT} = \left(E_{H_2O}^{DFT} - E_{H_2}^{DFT}\right) + \Delta H_{H_2O}^{exp} + \Delta E_{ZPE}^{exp}(H_2O - H_2 - \frac{1}{2}O_2)$, where $\Delta H_{H_2O}^{exp} = 241.81$ kJ mol^{-1}. Lastly, the charge density differences (CDD) plots shown in Fig. 2b) are calculated as: $\Delta\rho = (\rho_{CoO_x+support}^{relax} - \rho_{CoO_x}^{fixed} - \rho_{support}^{fixed})$, where ρ refers to calculated charge densities of the relaxed Co-oxide with support, only Co-oxide and only the support.

3 Results and Discussion

3.1 Synthesis at 1 × 10^{-6} mbar O_2

Figure 1 shows STM images representative of all types of cobalt oxide islands grown on Au(111), Pt(111) and Ag(111) in an oxygen pressure of 1 × 10^{-6} mbar (low oxygen pressure). As previously reported in an earlier study [18], two island morphologies, Co–O bilayers (∼90 %) and Co–O–Co–O double bilayers (∼10 %), coexist on the Au(111) surface at these preparation conditions. The termination of the layers was concluded on the basis of a comparison of STM images of the atomic structure and DFT calculations to be simple rock-salt like CoO for the bilayers, whereas the double bilayer islands adopted a wurtzite structure.

In direct comparison of the synthesis under the same conditions on Pt(111) (Fig. 1b), the bilayer structure is again concluded to be the prevailing island type, terminating the islands with a hexagonal atomic lattice in parallel with the substrate and displaying a hexagonal moiré pattern of larger periodicity, which is slightly rotated with respect to the basal plane CoO lattice atoms (as also reported on Au(111) [18]). On Pt(111), we measure an interatomic spacing from high-resolution STM images of the basal plane of 3.1 ± 0.1 Å which is slightly smaller than on Au(111) (∼3.3 Å [18]), but still very different from the Pt(111) lattice, which shows that heteroepitaxial film growth takes place on both substrates. The difference in the CoO lattice is also reflected in the moiré periodicity which can be roughly estimated to only 27 Å compared to 37 Å on the Au(111) substrate. In contrast to growth at low oxygen pressure on Au(111), bilayers are observed on Pt(111) together with thicker patches (2.9 ± 0.2 Å) showing the characteristics of O–Co–O trilayers [19]. The trilayers expose a $\sqrt{3} \times \sqrt{3}$R30° superstructure with respect to the underlying hexagonal CoO lattice, as revealed in high-resolution STM images (see Fig. 1b). We ascribe this to a partial hydroxyl overlayer (∼33 % coverage) present on this island type, in line with our recent observation of the same phenomenon on O–Co–O trilayers on Au(111) [19]. The trilayer patches are furthermore very similar in appearance to O–Fe–O iron oxide structures on Pt(111), where the same superstructure has been reported [37] and later ascribed to hydroxyls, possibly originating from background H_2 or H_2O residual gas [38]. Interestingly, as previously found on Au(111) [19], the underlying unit cell periodicity of the clean hexagonal O–Co–O lattice on Pt(111), as calculated from the $\sqrt{3} \times \sqrt{3}R30°$ periodicity of 4.6 ± 0.2 Å, results in 2.7 ± 0.2 Å indicating a 10 % contraction relative to the bilayer islands. This points to a pseudomorphic growth with the Pt(111) surface, also explaining the lack of moiré pattern on this island type.

In addition, the double bilayer structure observed on Au(111) at these preparation conditions was never found on Pt(111) under the synthesis conditions reported here. This points to a stronger interaction and, hence, wetting of CoO on Pt(111) compared with Au(111). We note, that this effect facilitates the preparation of a completely homogeneous bilayer film which we never accomplished on Au(111) due to formation of double bilayer domains.

On Ag(111), the most striking finding is the absence of the bilayer morphology which does not appear to be stabilized at our experimental conditions in contrast to the preferred bilayer growth on both Au(111) and Pt(111). In general, flat and crystalline island structures were only

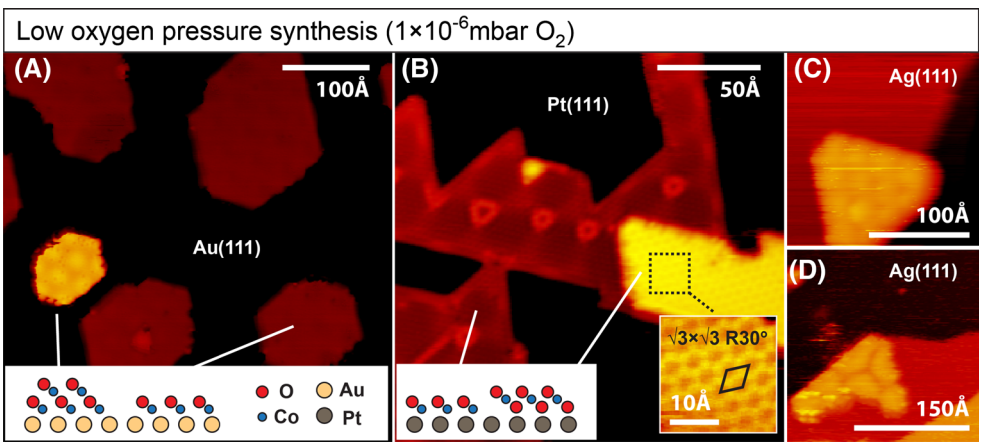

Fig. 1 Growth of cobalt oxide nanoislands at 1 × 10^{-6} mbar O_2 on Au(111) (**a**), Pt(111) (**b**), and Ag(111) (**c, d**). The ball model *insets* show side views of the synthesized structures: Co–O bilayer (Au(111) and Pt(111)), Co–O–Co–O double bilayer (Au(111)), and O–Co–O trilayer (Pt(111)). Imaging parameters: (**a**)−1486.5 mV/0.210 nA, (**b**)−743.1 mV/0.370 nA, (**c**)−1317.1 mV/0.280 nA, and (**d**)−1062.3 mV/0.260 nA

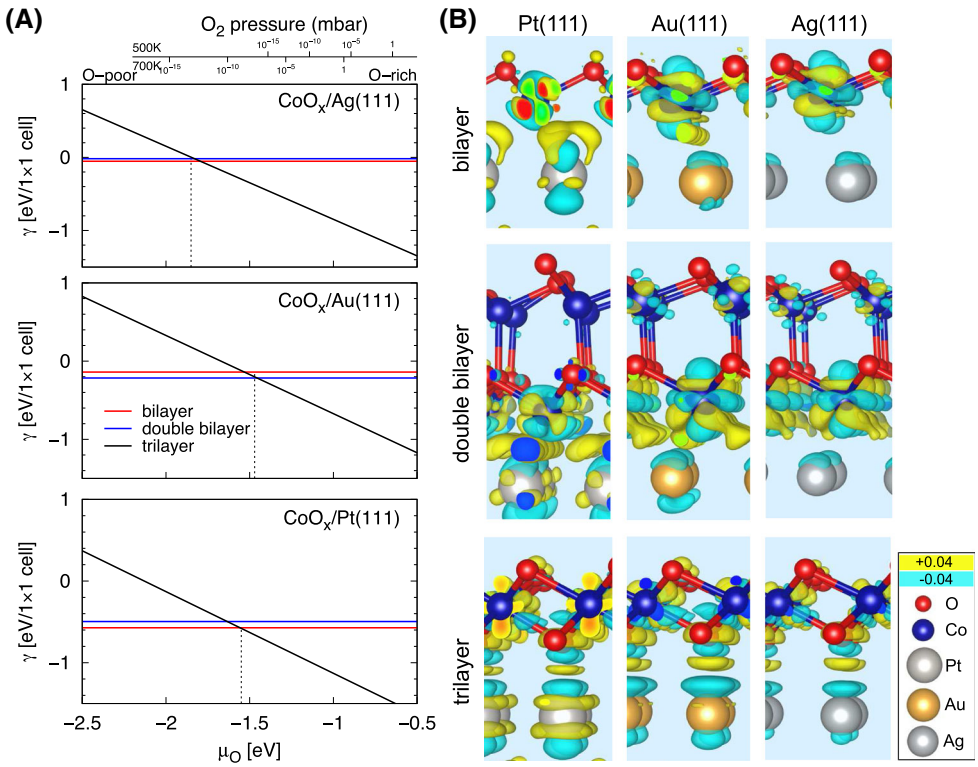

Fig. 2 **a** Calculated stability diagrams in terms of surface energy $\Delta\gamma$ for three types infinite oxide layers supported on Pt(111), Au(111) and Ag(111) as function of oxygen chemical potential. The $p(T)$ scale is also shown for reference. **b** Comparison of the charge transfer levels in these systems relative to unsupported oxides obtained from charge–density difference plots

found attached to step edges of the Ag(111) surface (Fig. 1c, d), which indicates a notably weaker interaction with the Ag(111) compared with Au(111) and Pt(111). The islands consist of two differing types, both with a hexagonal ordering of the basal plane atoms with a periodicity roughly determined to 3.1 ± 0.3 Å as measured by atomic resolution STM images. The characteristics of the first island type (Fig. 1c) are in agreement with the double bilayers (Co–O–Co–O) observed on Au(111) with a strong corrugated moiré pattern and an apparent height of 3.8 ± 0.2 Å, matching the 4.0 Å measured in [18]. The second morphology, embedded in the Ag(111) step edges (Fig. 1d), displays an irregular moiré pattern and a different apparent height of 4.7 ± 0.2 Å. We speculate that the structure of this island type could be either a O–Co–O–Co–O multilayer as described in [19] (see also Sect. 3.2) or spinel cobalt oxide in the (111) termination, as suggested previously for similar CoO_x islands on Au(111) [39]. We note, that the observed preferential growth of cobalt oxides on the step edges has also previously been reported in case of a step decoration growth of CoO nanostructures on a vicinal Pd(100) surface [40].

3.1.1 Theoretical Stability Calculations

The thermodynamic stability of the supported Co-oxide films was assessed by DFT calculations (see also Sect. 2.2 on Computational details). Our results are summarized in Fig. 2a, where we plot the surface energy per 1 × 1 area of infinite (i.e. a continuous film of-) bilayer, double bilayer and trilayer structures as supported on Pt(111), Au(111) and Ag(111). It is clear, that at oxygen poor conditions, $\mu_O < -2$ eV, the bilayers and double bilayers are the most stable oxide structures. Their relative stability is largest on the Pt(111) support followed by Au(111) and then Ag(111), where it is nearly unstable when compared to CoO-bulk in very good agreement with our experimental findings. For Au(111), the double-bilayer is marginally more stable than single bilayers while the opposite is true for Pt(111), which might explain why double bilayers are only found to coexist with the bilayer structure on Au(111). The reason behind this difference in stability is likely due to much larger compressive strain in case of Pt(111) as compared to Au(111) (as seen in our current study [31]), which affects double bilayers more than single bilayers and results in the visible symmetry breaking of the double-bilayer structure [see Fig. 2b for Pt(111)]. At oxygen rich conditions, $\mu_O > -1.4$ eV, the trilayer is predictively the most stable oxide structure. The relative stability indicates trilayers on the Pt(111) support as the most stable followed first by Ag(111) and then by Au(111). We therefore predict Ag(111) supported trilayers to be more stable than on Au(111). The transition at which bilayers change to

Table 1 Bader charge analysis of the electronic charge transferred towards the support per (1 × 1) area

Co-oxide	Pt(111)	Au(111)	Ag(111)
Bilayer	0.240	0.194	0.083
Double bilayer	0.271	0.245	0.126
Trilayer	−0.263	−0.219	−0.248

The positive (negative) values indicate electron excess (depletion) in the support which leads to a more oxidized (reduced) metal-oxide layer

trilayers happens at lower oxygen potentials (i.e. lower O_2 pressures) for Pt(111) than for Au(111), also in agreement with experimental observations.

In addition to energetics and structural properties, the electronic properties such as charge transfer interactions between metal oxide and support are of high interest to fundamental understanding and to possible future applications. The charge density differences (CDD) plots for our structures are shown in Fig. 2b, while the detailed list of the transferred charge is listed in Table 1. From these plots and from the charge analysis in Table 1, it is clear that Pt(111) has by far the largest interaction with the Co-oxide overlayers, which is oxidizing for bilayers (as seen in our current study [31]) and reducing for the trilayers (as seen before in our study [18]). Again, following the trends obtained for the energetics, these effects are smaller for Au(111) and Ag(111) bilayers. However, the trilayers on Ag(111) are found to be more strongly interacting than on Au(111).

3.2 Synthesis at >1 × 10^{-5} mbar O_2

At elevated oxygen pressure (>1 × 10^{-5} mbar O_2), the cobalt oxide morphology changes towards more oxygen rich structures. The structures formed on Au(111) (described in further detail in [19]) are shown in the STM images in Fig. 3a–c and consist of O–Co–O trilayers (see also Sect. 3.1) at 400 K. For a temperature above 573 K exclusively O–Co–O–Co–O multilayers are formed. Similarly, on Pt(111) we observe islands displaying the characteristics of O–Co–O trilayers at 400 K (Fig. 3d), and as on Au(111), these islands can be converted into O–Co–O–Co–O multilayers at a higher temperature (Fig. 3e, f), identified by the strong moiré pattern and an apparent height of roughly 5 Å which is close to the 4.6 Å measured on Au(111) in [19]. However, it was found that a higher temperature of 723 K was needed to fully convert the trilayer structure to multilayers on Pt(111) compared to Au(111), where a full conversion is already accomplished at 573 K. Consequently, annealing to an intermediate temperature results in a mixture of the trilayer- and multilayer morphologies on Pt(111) as shown in Fig. 3e. In line with our DFT results (Sect. 3.1.1), we speculate that the particularly high stability of bilayers and trilayers on Pt(111) and the strong interaction with this substrate might

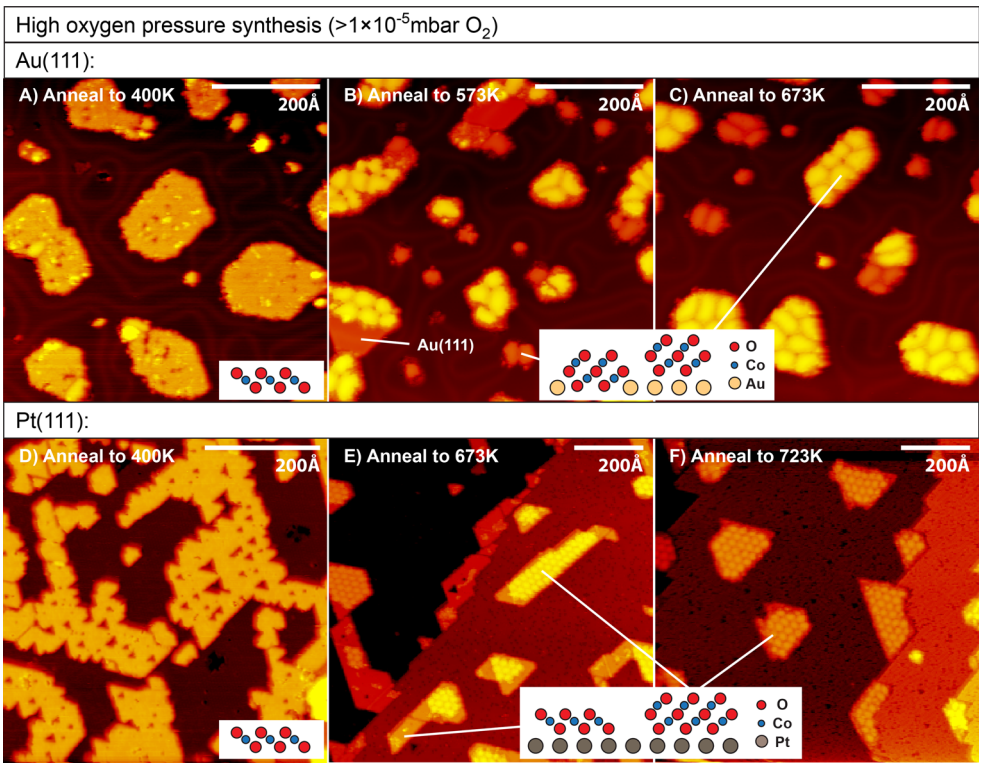

Fig. 3 Cobalt oxide islands on Au(111)/Pt(111) at elevated oxygen pressure. (**a** + **d**) Low temperature annealing (400 K) produces trilayer islands, whereas the multilayer structure dominates at higher temperatures (**b, c** and **e, f**). Ball model side views are shown in the *insets*. At an intermediate temperature of 673 K, trilayers and multilayers are coexisting on Pt(111) (**e**). Note also that a small proportion of the multilayers on Au(111) are buried one layer into the Au(111) surface. Imaging parameters: **a** 1489.9 mV/0.190 nA, **b** −1444.1 mV/0.130 nA, **c** −1441.1 mV/0.160 nA, **d** −275.3 mV/0.280 nA, **e** −1225.3 mV/0.290 nA, and **f** −1051.0 mV/0.330 nA

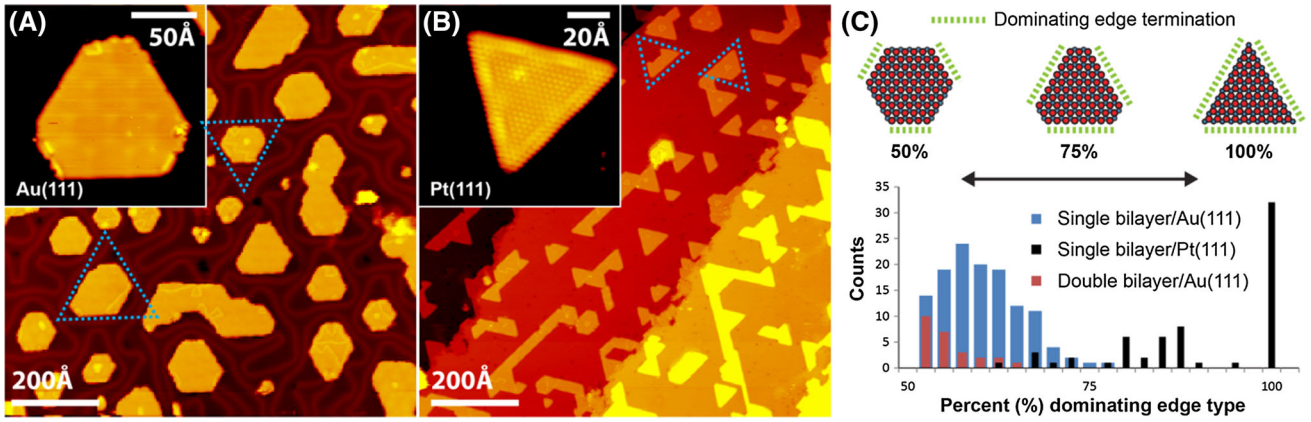

Fig. 4 Single bilayer islands on Au(111) and Pt(111): Overview STM images (**a, b**) and island shape distribution from 216 islands analyzed from STM images in terms of percent dominating edge type, where 50 and 100 % corresponds to a *regular hexagon* and a *perfect triangle* respectively (**c**). *Blue dotted triangles* indicate two possibilities of island orientations with respect to the substrate. Imaging parameters: **a** −883.8 mV/0.340 nA (*inset* −939.6 mV/0.240 nA), **b** −1041.5 mV/0.270 nA (*inset* 670.5 mV/0.320 nA)

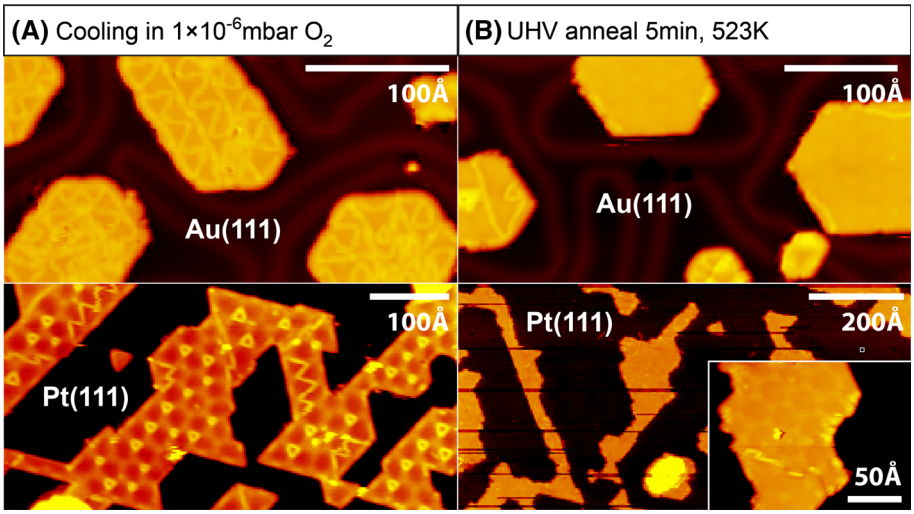

Fig. 5 Incorporation of defect lines in bilayer islands on Au(111) and Pt(111). **a** The density can be increased by cooling in O_2 after synthesis. **b** Removal of defect lines by UHV annealing. Imaging parameters: **a** −1071.8 mV/0.220 nA (*upper*), −743.1 mV/0.280 nA (*lower*), **b** −1095.6 mV/0.200 nA (*upper*), −1129.7 mV/0.260 nA (*lower*), −1129.7 mV/0.330 nA (*inset*)

explain the higher temperature needed to restructure the bilayer- and trilayer islands into stacked multilayers.

3.3 Comparison of Bilayer Growth on Au(111) and Pt(111)

We now turn our attention to the morphology and edge structure of the bilayer islands on Pt(111) and Au(111). Representative overview STM images of syntheses at low oxygen pressure are shown in Fig. 4a, b for comparison. The growth is seen to be dominated by the bilayer structure on both substrates.

3.3.1 Stacking Fault Defect Lines in the Bilayer Structure

A useful feature when addressing the island edge structure (see Sect. 3.3.2) is the appearance of linear defect lines, often referred to as dislocation lines, in the bilayer structure, observed on both Au(111) and Pt(111). Figure 5a shows STM images of bilayer islands exposed to an oxidizing treatment by cooling the sample to 350 K in 1×10^{-6} mbar O_2 after ended synthesis procedure. On both substrates, the abundance of defect lines in the island basal planes is seen to be highly promoted by this procedure. Contrary, annealing to 523 K in UHV (Fig. 5b) has the effect of removing the defect lines, proceeding gradually over time until almost no defect lines can be observed. We therefore conclude that the defect lines are connected with incorporation of excess oxygen in the island structure that can easily be removed again by exposure to reducing conditions (UHV annealing).

Linear defects in a CoO(111) monolayer film on Pt(111) have previously been reported, however the observed defect lines were created under reducing conditions by insufficient oxidation of the film [16], and the structural model proposed was accordingly oxygen deficient

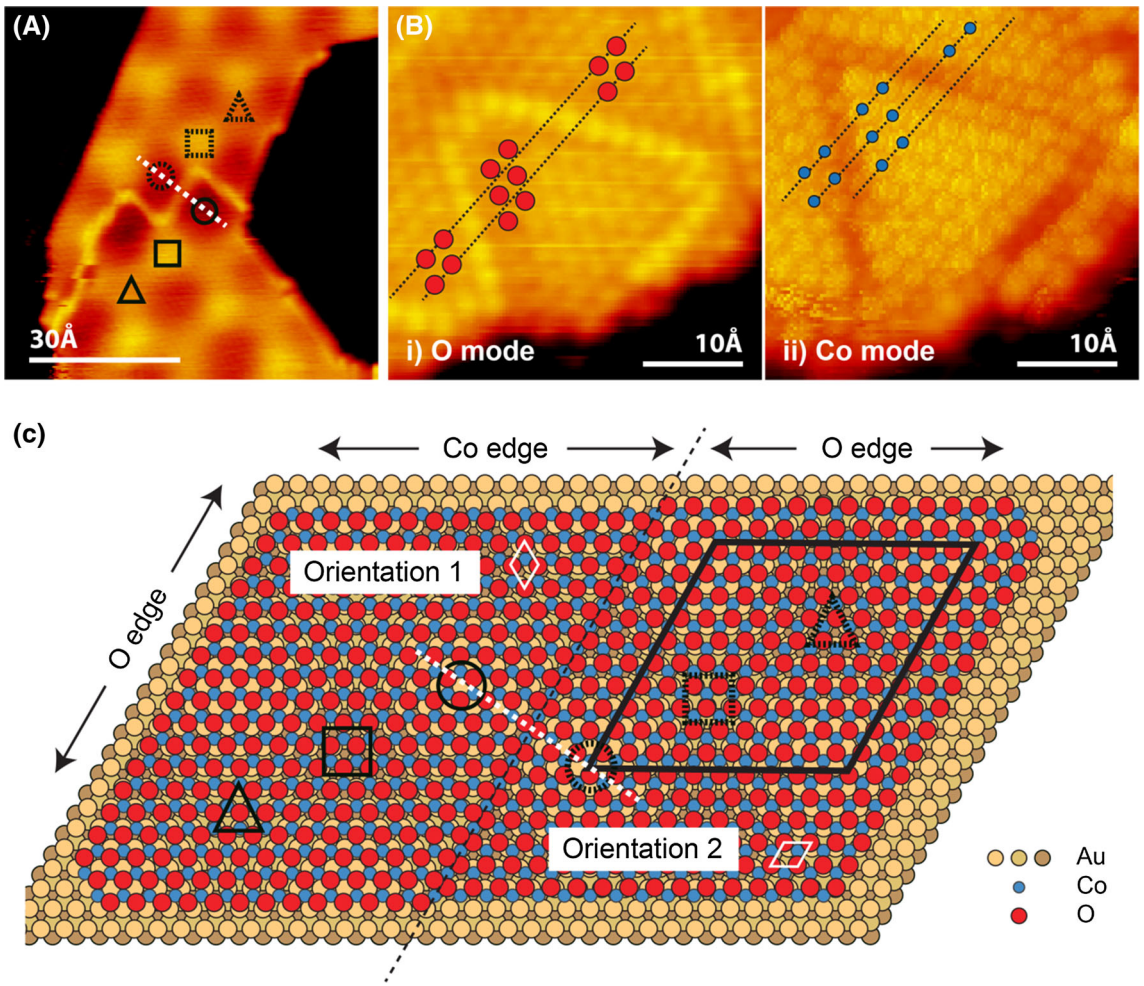

Fig. 6 **a** Assignment of three distinguishable domain types in the moiré structure (CoO bilayer/Au(111)). The sequence changes when a defect line is crossed. **b** STM images of the same defect line loop in two different imaging modes, displaying the oxygen lattice (O mode) (i) and cobalt lattice (Co mode) (ii) respectively (CoO bilayer/Au(111)). **c** Structural model of a defect line corresponding to the observed defect lines, demonstrating the consequences for edge types and moiré domains when crossing the line. Note that this type of line defect is parallel to oxygen edges (O edges). The *triangle*, *square* and *circle* represent domains with different Au–Co–O stacking sequences (see text). Imaging parameters: **a** −1095.6 mV/0.220 nA, **b** −362.8 mV/0.490 nA (O mode) and −670.5 mV/0.320 nA (Co mode)

compared to the pristine film. Similar structures were beforehand observed and described in detail on FeO thin films on Pt(111) by reducing the film with atomic hydrogen [25]. In line with analysis performed from STM images on the FeO system [25, 26], we propose the different structural model in Fig. 6c for the defect lines observed on our bilayer islands on both Au(111) and Pt(111)—a structure that has also been observed under oxidizing conditions on FeO thin films supported on Pd(111) [41] and FeO islands on Pt(111) [26].

As illustrated in the ball model (Fig. 6c), the defect lines are formed at the boundary between domains of different orientations of the CoO film on the substrate. The two orientations of the CoO(111) film relative to the underlying Au(111) are differentiated by a 60° rotation (both unit cells are indicated by the white rhombe in Fig. 6c) or, equivalently, the movement of every oxygen atom to the nearby hollow site.

To confirm the proposed model, we analyzed the STM images in Fig. 6b of the same defect line, recorded in two different STM imaging modes originating from the high sensitivity of the STM contrast formation on oxide surfaces to tip termination [42]. In the first mode (mode i, most common) the defect line appears bright, whereas it shows up as a depression in the second mode (mode ii). By superimposing a number of guide lines on the images, it is revealed that the imaged basal plane atoms are either *out of* registry (mode i) or *in* registry (mode ii) respectively when crossing the defect line. In line with this observation, we interpret the two imaging modes as showing the oxygen- and cobalt lattices respectively (O mode/Co mode), in agreement with the model in Fig. 6c where the underlying

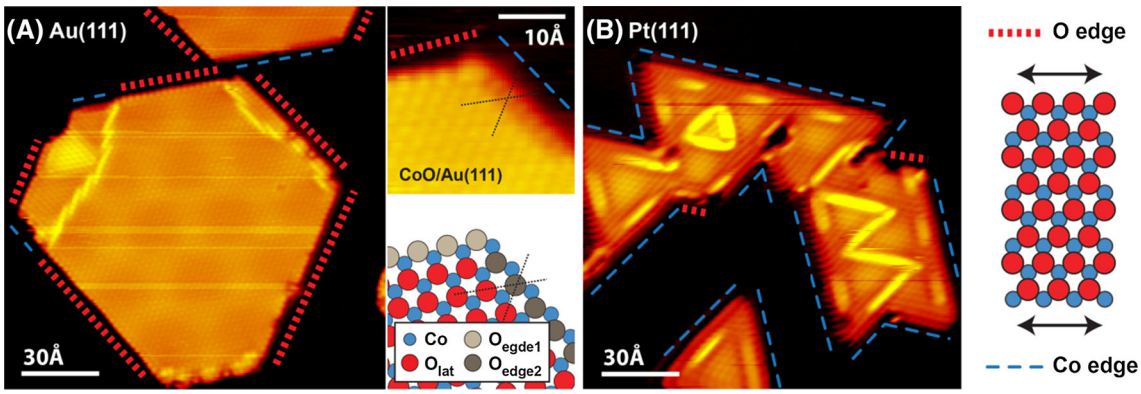

Fig. 7 Assignment of edge types in CoO bilayer islands using defect lines on Au(111) (**a**) and Pt(111) (**b**). O terminated edges (O edges) are marked by *red dotted lines* and cobalt terminated edges (Co edges) by *blue striped lines*. Imaging parameters: **a** −1095.6 mV/0.240 nA (both images) and **b** −743.1 mV/0.370 nA

cobalt lattice is unaffected by the presence of the defect line, but oxygen atoms are shifted to nearby hollow sites from one orientation to the other. Alternatively, the lattice out of registry could in principle be the Co lattice. However, this interpretation would not result in additional incorporation of oxygen, and therefore not intuitively explained by our observation of promotion of defect lines under oxidative conditions.

Figure 6c also shows the resulting moiré pattern due to the lattice mismatch between the in-plane interatomic spacings in the CoO(111)- and Au(111) surfaces. This gives rise to three characteristic domain types on each film orientation (6 types in total, marked with full line/dotted triangles, squares and circles respectively). In "orientation 1" these are denoted FCC, HCP and TOP, referring to the CoO stacking sequence with respect to the Au(111) underneath (see Ref. [25] for structural models in the case of FeO on Pt(111)). Similarly, the three domain types in "orientation 2" are referred to as FCC-like, HCP-like and TOP-like since they are identical to the FCC, HCP and TOP domains in if only the top layer of Au(111) is taken into account.

The analysis of moiré patterns predicts that the sequence of domain types along a specific direction is reversed when crossing a defect line from one film orientation to the other. As can be seen in the image in Fig. 6a, the moiré patterns appear similarly in STM (one bright (square)-, one dark (circle)- and one intermediate (triangle) contrast on both orientations separated by the defect line. This can be understood assuming that the deeper Au layers only have a minor effect on the STM contrast formation such that FCC/FCC-like areas display the same contrast etc. In this way, the sequence of domain types is shown to change across the defect line in Fig. 6a in agreement with the structural model (Fig. 6c). Furthermore, the white dotted line in the model indicates that the same domain type should be found on both sides of the defect line, as observed in the STM image, Fig. 6a.

Finally, we note that the possibility for each island to exist in one of the two CoO(111) film orientations, "1" or "2", immediately explains the presence of "UP"- and "DOWN" pointing islands in STM overview images (indicated in Fig. 4a, b), as the 60° rotation of an island with a fixed structure and (here triangular) shape would indeed result in a change from "UP" to "DOWN" or vice versa (see supplementary figure S2).

3.3.2 *Edge Structure of Au(111)- and Pt(111) Supported Bilayer Islands*

With the structural model in Fig. 6c established, the defect lines can be exploited in the assignment of edge types. As can be seen in the figure, the line dislocations are parallel to oxygen terminated edges. Parallel edges on opposite sides of an island display opposite edge structure, i.e. oxygen-/cobalt terminated edges respectively. Furthermore, when passing a 120° corner along the island edge, as well as crossing a defect line pointing into the edge structure (as exemplified in the figure), the edge type similarly changes. Finally, passing a 60° island corner results in no change of edge type.

Figure 7a shows an example of CoO islands on Au(111) in which defect lines are used to assign all edges as either oxygen- or cobalt terminated edges (O-/Co edges) according to the rules stated above. Interestingly, it is also possible to distinguish the edge types by means of STM where O edges appear bright and Co edges display a dark zone along the edge direction. Both STM images in Fig. 7a were recorded in the same imaging mode as earlier denoted the "O mode" (Fig. 6b), hence showing the oxygen lattice, which is consistent with the finding that the protrusions along both O- and Co edges are *in* registry with the basal

plane O atoms (see the high-magnification STM image in Fig. 7a). The observed change in STM contrast from one edge type to the other is likely to be related to the change in chemical environment of the O atoms ($O_{lat}/O_{edge1}/O_{edge2}$) shown in the ball model (Fig. 7a).

On Pt(111) the prevailing edge type is seen to be the cobalt terminated edge (Fig. 7b). This edge type has a linear feature parallel to the edge appearing with a periodicity of the moiré pattern, creating a characteristic "road makings" motif, as can be seen the STM image, Fig. 7b. The few oxygen terminated edges in this image are irregular and no high-resolution images of intact O edges was acquired on Pt(111). Measuring the O- and Co edge lengths on islands from a large sample area yields ~91 % cobalt terminated edges which is in contrast to the same measurement on Au(111), yielding a Co edge abundance of only 39 %. Hence, the Co edge structure seems to be strongly favored on Pt(111) and slightly unfavored on Au(111).

We also note that the favoring of one edge type over the other is a driving force behind the island shape formation on both substrates, explaining the predominance of hexagons exposing both Co and O edges on Au(111) towards weakly truncated triangles on Pt(111) terminated by long Co edges. As the considered oxygen- and metal ion terminated edges are polar (equivalent to the MgO nanoribbons in [43]), the stabilizing ability of the substrate to screen the edge charges of the two edge terminations respectively may be different from Au(111) to Pt(111) and hence explain the difference in relative abundances. In particular, analysis of the edge structure of the minority double bilayers on Au(111) (see [18]) reveals that all edges consist of both the oxygen- and cobalt terminations on top of each other (however changing between the top/bottom positions), resulting in a nonpolar edge termination. This, in turn, suggests a lack of edge type preference, providing a possible explanation of the shape distribution towards regular hexagons in the histogram (Fig. 4c).

4 Conclusions

Based on STM experiments and DFT calculations, our results indicate that at low oxygen pressure (1×10^{-6} - mbar O_2): (1) The Co–O bilayer morphology is the dominating phase on Au(111) and Pt(111), but not easily stabilized on Ag(111), (2) the transition point from Co–O bilayers to O–Co–O trilayers is situated at a lower oxygen pressure on Pt(111) as compared to Au(111) and (3) Co–O–Co–O double bilayers are unfavored in the growth on Pt(111) whereas this island type is coexisting with bilayers on Au(111). At an elevated temperature and high oxygen pressure ($>1 \times 10^{-5}$ mbar O_2), transition to O–Co–O–Co–O multilayers is observed on both Au(111) and Pt(111), however a full conversion on Pt(111) requires a higher temperature (723 K) than on Au(111) (573 K) which we assign to the high stability of the precursor bilayers on Pt(111) according to our DFT calculations.

Interestingly, we observe a change in the bilayer island shape between the Au and Pt substrates from irregular hexagons on Au(111) towards triangles on Pt(111). This tendency is revealed to be related to the edge structure, displaying 91 % of the favored Co metal edge type on Pt compared to only 39 % on Au. Since the Co terminated edge type is likely to host the active sites for water dissociation and CO oxidation etc., we highlight that such an effect of the substrate could be of interest in the development of new effective catalyst designs based on Co oxide/noble metal systems.

Acknowledgments The iNANO group gratefully acknowledges support from the Lundbeck Foundation and Villum Foundation. MB, PNP and AV gratefully acknowledge support from the U.S. Department of Energy Office of Basic Energy Science to the SUNCAT Center for Interface Science and Catalysis. AV acknowledges the support from the SLAC National Accelerator Lab LDRD program. MB, PNP and AV would like to acknowledge the use of the computer time allocation for the "Computational search for highly efficient 2d and 3d nano-catalysts for water splitting" at the National Energy Research Scientific Computing Center, a DOE Office of Science User Facility supported by the Office of Science of the U.S. Department of Energy under Contract No. DE-AC02-05CH11231. ZS would like to acknowledge the financial support from the Chinese Scholarship Council (CSC).

References

1. Xie X, Li Y, Liu Z-Q, Haruta M, Shen W (2009) Low-temperature oxidation of CO catalysed by Co_3O_4 nanorods. Nature 458(7239):746–749
2. Ren Y, Ma Z, Qian L, Dai S, He H, Bruce PG (2009) Ordered crystalline mesoporous oxides as catalysts for CO oxidation. Catal Lett 131(1–2):146–154
3. Liao L, Zhang Q, Su Z, Zhao Z, Wang Y, Li Y, Lu X, Wei D, Feng G, Yu Q (2014) Efficient solar water-splitting using a nanocrystalline CoO photocatalyst. Nat Nanotechnol 9(1):69–73
4. Song F, Hu X (2014) Exfoliation of layered double hydroxides for enhanced oxygen evolution catalysis. Nat Commun. doi:10.1038/ncomms5477
5. Rosen J, Hutchings GS, Jiao F (2013) Ordered mesoporous cobalt oxide as highly efficient oxygen evolution catalyst. J Am Chem Soc 135(11):4516–4521
6. Liotta LF, Wu H, Pantaleo G, Venezia AM (2013) Co_3O_4 nanocrystals and Co_3O_4–MO_x binary oxides for CO, CH_4 and VOC oxidation at low temperatures: a review. Catal Sci Technol 3(12):3085–3102
7. Lu X, Ng YH, Zhao C (2014) Gold nanoparticles embedded within mesoporous cobalt oxide enhance electrochemical oxygen evolution. ChemSusChem 7(1):82–86
8. Yeo BS, Bell AT (2011) Enhanced activity of gold-supported cobalt oxide for the electrochemical evolution of oxygen. J Am Chem Soc 133(14):5587–5593

9. De Chialvo MG, Chialvo A (1993) Oxygen evolution reaction on $Ni_xCo_{(3-x)}O_4$ electrodes with spinel structure. Electrochim Acta 38(15):2247–2252
10. Wu G, Li N, Zhou D-R, Mitsuo K, Xu B-Q (2004) Anodically electrodeposited Co + Ni mixed oxide electrode: preparation and electrocatalytic activity for oxygen evolution in alkaline media. J Solid State Chem 177(10):3682–3692
11. Lin P-Y, Skoglundh M, Löwendahl L, Otterstedt J-E, Dahl L, Jansson K, Nygren M (1995) Catalytic purification of car exhaust over cobalt- and copper-based metal oxides promoted with platinum and rhodium. Appl Catal B 6(3):237–254
12. Törncrona A, Skoglundh M, Thormählen P, Fridell E, Jobson E (1997) Low temperature catalytic activity of cobalt oxide and ceria promoted Pt and Pd: -influence of pretreatment and gas composition. Appl Catal B 14(1):131–145
13. Meyer W, Biedermann K, Gubo M, Hammer L, Heinz K (2008) Surface structure of polar Co_3O_4(111) films grown epitaxially on Ir(100)-(1 × 1). J Phys 20(26):265011
14. Heinz K, Hammer L (2013) Epitaxial cobalt oxide films on Ir(100)—the importance of crystallographic analyses. J Phys 25(17):173001
15. Gragnaniello L, Agnoli S, Parteder G, Barolo A, Bondino F, Allegretti F, Surnev S, Granozzi G, Netzer F (2010) Cobalt oxide nanolayers on Pd(100): the thickness-dependent structural evolution. Surf Sci 604(21):2002–2011
16. De Santis M, Buchsbaum A, Varga P, Schmid M (2011) Growth of ultrathin cobalt oxide films on Pt(111). Phys Rev B 84(12):125430
17. Li M, Altman E (2014) Shape, morphology, and phase transitions during co oxide growth on Au(111). J Phys Chem C 118(24):12706–12716
18. Walton AS, Fester J, Bajdich M, Arman MA, Osiecki J, Knudsen J, Vojvodic A, Lauritsen JV (2015) interface controlled oxidation states in layered cobalt oxide nanoislands on gold. ACS Nano 9(3):2445–2453
19. Fester J, Walton AS, Li Z, Lauritsen JV, Gold-supported two-dimensional cobalt oxyhydroxide (CoOOH) and multilayer cobalt oxide islands (submitted)
20. Ferstl P, Mehl S, Arman M, Schuler M, Toghan A, Laszlo B, Lykhach Y, Brummel O, Lundgren E, Knudsen J (2015) Adsorption and activation of CO on Co_3O_4(111) thin films. J Phys Chem C 119(29):16688–16699
21. Sun YN, Giordano L, Goniakowski J, Lewandowski M, Qin ZH, Noguera C, Shaikhutdinov S, Pacchioni G, Freund HJ (2010) The interplay between structure and CO oxidation catalysis on metal-supported ultrathin Oxide films. Angew Chem 122(26):4520–4523
22. Freund H-J (2007) Metal-supported ultrathin oxide film systems as designable catalysts and catalyst supports. Surf Sci 601(6):1438–1442
23. Fu Q, Li W-X, Yao Y, Liu H, Su H-Y, Ma D, Gu X-K, Chen L, Wang Z, Zhang H (2010) Interface-confined ferrous centers for catalytic oxidation. Science 328(5982):1141–1144
24. Rodriguez J, Ma S, Liu P, Hrbek J, Evans J, Perez M (2007) Activity of CeO_x and TiO_x nanoparticles grown on Au(111) in the water-gas shift reaction. Science 318(5857):1757–1760
25. Merte LR, Knudsen J, Grabow LC, Vang RT, Lægsgaard E, Mavrikakis M, Besenbacher F (2009) Correlating STM contrast and atomic-scale structure by chemical modification: vacancy dislocation loops on FeO/Pt(111). Surf Sci 603(2):L15–L18
26. Zeuthen H, Kudernatsch W, Merte LR, Ono LK, Lammich L, Besenbacher F, Wendt S (2015) Unraveling the edge structures of platinum (111)-supported ultrathin FeO islands: the influence of oxidation state. ACS Nano 9(1):573–583
27. Besenbacher F, Lægsgaard E, Mortensen K, Nielsen U, Stensgaard I (1988) Compact, high-stability, ''thimble-size'' scanning tunneling microscope. Rev Sci Instrum 59(7):1035–1038
28. Kresse G, Hafner J (1993) Ab initio molecular dynamics for liquid metals. Phys Rev B 47(1):558
29. Kresse G, Joubert D (1999) From ultrasoft pseudopotentials to the projector augmented-wave method. Phys Rev B 59(3):1758
30. Kresse G, Furthmüller J (1996) Efficiency of ab initio total energy calculations for metals and semiconductors using a plane-wave basis set. Comput Mater Sci 6(1):15–50
31. Plessow PN, Bajdich M, Greene J, Vojvodic A, Abild-Pedersen F (2016) Trends in thermodynamic stability of ultrathin supported oxide films. J Phys Chem C. doi:10.1021/acs.jpcc.6b01404
32. Perdew JP, Burke K, Ernzerhof M (1996) Generalized gradient approximation made simple. Phys Rev Lett 77(18):3865
33. Dudarev S, Botton G, Savrasov S, Humphreys C, Sutton A (1998) Electron-energy-loss spectra and the structural stability of nickel oxide: an LSDA + U study. Phys Rev B 57(3):1505
34. Nilius N, Benedetti S, Pan Y, Myrach P, Noguera C, Giordano L, Goniakowski J (2012) Electronic and electrostatic properties of polar oxide nanostructures: MgO(111) islands on Au(111). Phys Rev B 86(20):205410
35. Giordano L, Pacchioni G, Goniakowski J, Nilius N, Rienks ED, Freund H-J (2007) Interplay between structural, magnetic, and electronic properties in a FeO/Pt(111) ultrathin film. Phys Rev B 76(7):075416
36. Reuter K, Scheffler M (2001) Composition, structure, and stability of RuO_2(110) as a function of oxygen pressure. Phys Rev B 65(3):035406
37. Giordano L, Lewandowski M, Groot I, Sun Y-N, Goniakowski J, Noguera C, Shaikhutdinov S, Pacchioni G, Freund H-J (2010) Oxygen-induced transformations of an FeO(111) film on Pt(111): a combined DFT and STM study. J Phys Chem C 114(49):21504–21509
38. Johansson N, Merte LR, Grånäs E, Wendt S, Andersen JN, Schnadt J, Knudsen J (2016) Oxidation of ultrathin FeO(111) grown on Pt(111): spectroscopic evidence for hydroxylation. Top Catal. doi:10.1007/s11244-015-0521-7
39. Li M, Altman E (2014) Cluster-size dependent phase transition of Co oxides on Au(111). Surf Sci 619:L6–L10
40. Ma L-Y, Picone A, Wagner M, Surnev S, Barcaro G, Fortunelli A, Netzer FP (2013) Structure and electronic properties of CoO nanostructures on a vicinal Pd(100) surface. J Phys Chem C 117(36):18464–18474
41. Zeuthen H, Kudernatsch W, Peng G, Merte LR, Ono LK, Lammich L, Bai Y, Grabow LC, Mavrikakis M, Wendt S (2013) Structure of stoichiometric and oxygen-rich ultrathin FeO(111) films grown on Pd(111). J Phys Chem C 117(29):15155–15163
42. Mönig H, Todorovic M, Baykara MZ, Schwendemann TC, Rodrigo L, Altman EI, Perez R, Schwarz UD (2013) Understanding scanning tunneling microscopy contrast mechanisms on metal oxides: a case study. ACS Nano 7(11):10233–10244
43. Goniakowski J, Giordano L, Noguera C (2013) Polarity compensation in low-dimensional oxide nanostructures: the case of metal-supported MgO nanoribbons. Phys Rev B 87(3):035405